Batteries & Supercaps

Research Article
doi.org/10.1002/batt.202400231

Chemistry Europe
European Chemical Societies Publishing

www.batteries-supercaps.org

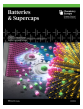

Compatibility of Molybdenum Disulfide and Magnesium Fluorinated Alkoxyaluminate Electrolytes in Rechargeable Mg Batteries

Omar Falyouna,*[a] Mohd Faizul Idham,[b] Osama Eljamal,[c] and Toshihiko Mandai*[a, d]

Molybdenum disulfide (MoS_2)-based cathodes have exhibited good electrochemical reactions in all phenyl complex (APC) electrolytes. However, APC electrolytes are highly corrosive and susceptible to oxidation. Alternatively, magnesium fluorinated alkoxyaluminate electrolyte ($Mg[Al(HFIP)_4]_2$) is a pioneering chloride-free electrolyte with remarkable electrochemical activity in rechargeable Mg batteries (RMBs). This study aims to investigate the compatibility of various MoS_2 nanomaterials with $Mg[Al(HFIP)_4]_2$ in RMBs. Seven MoS_2 nanomaterials were synthesized under different hydro/solvothermal conditions and evaluated as cathode materials in RMBs. The results revealed that the electrochemical activity of the as-synthesized MoS_2 in RMBs significantly varied and MoS_2 with high content of 1T-phase (M5) exhibited the best specific capacity of ca. 35 mAh g^{-1}. Heteroatom doping, graphene oxide (GO) incorporation, and dual-salt electrolytes were employed to enhance the electrochemical performance of M5. The electrochemical tests showed that all doped-MoS_2 and GO-MoS_2 delivered poor specific capacities (<20 mAh g^{-1}), properly due to the disorder of the cathode material and the entrapment of Mg^{2+} ions. In contrast, dual-salt electrolytes (0.3 M $Mg[Al(HFIP)_4]_2$/0.3 M LiCl) improved the initial specific capacity by 242%. This is attributed to the preferential intercalation of Li^+ ions that reduces the diffusion energy barrier and facilitates the intercalation of Mg^{+2} ions.

1. Introduction

Nowadays, owing to their remarkable energy density and cycling stability, LIBs are widely used in various portable electronic devices, e.g., cameras, laptops, mobile phones, etc..[1–3] However, the development of next-generation LIBs is hindered by several issues related to safety and cost. For example, Li metal anodes are suspectable to thermal runaway due to the growth of dendrites.[4] Furthermore, the scarcity of natural lithium resources (0.0017 wt% in earth's crust, Table S1) increases the prices of LIBs.[2] Rechargeable magnesium batteries (RMBs) are one of the promising post-LIBs because of their high theoretical specific capacity (i.e., 2205 mAh g^{-1}).[5,6] The superior characteristics of RMBs over LIBs stem from the intrinsic properties of Mg. For instance, Mg is highly abundant in the earth's crust (2.1 wt%, Table S1) and inexpensive (2700 $/ton of Mg *vs.*64,800$/ton of Li) which opens the door for a novel storage technology with a specific energy capacity (3833 mAh cm^{-3} *vs.* 2046 mAh cm^{-3} for LIBs) suitable for large-scale applications at affordable prices.[7,8] Moreover, RMBs are more environmentally friendly and safer than LIBs because metallic Mg is stable when exposed to air and doesn't form dendrites under reversible electrochemical reactions.[9] Nevertheless, the development of RMBs faces two critical challenges. The first challenge is the sluggish diffusion of Mg^{2+} ions in the cathode material due to the high charge density of the divalent Mg^{2+}.[10,11] The second challenge is that most of the suitable electrolytes for RMBs promote the formation of a surface passivation layer that inhibits further electrochemical reactions.[12] Therefore, current research efforts are devoted to finding compatible cathode materials and electrolytes that allow the fast insertion/extraction of Mg^{2+} and prevent the formation of passivation layers on the surface of the Mg anode.

Molybdenum disulfide (MoS_2), a well-known layered transition metal dichalcogenide, has been extensively used as excellent electrode material in many battery applications because of its unique layered structure that facilitates the intercalation/deintercalation of single and multivalent ions such as lithium (Li),[13,14] sodium (Na),[15,16] zinc (Zn),[17,18] etc. Furthermore, several studies demonstrated that MoS_2-based cathode materials promoted the intercalation/deintercalation of divalent

[a] O. Falyouna, T. Mandai
Center for Advanced Battery Collaboration, Research Center for Energy and Environmental Materials, National Institute for Materials Science, 1-1 Namiki, Tsukuba, Ibaraki, 305-0044, Japan
E-mail: falyouna.omar@nims.go.jp
mandai.toshihiko@nims.go.jp

[b] M. Faizul Idham
School of Mechanical Engineering, College of Engineering, Universiti Teknologi MARA, 23000 Cawangan Terengganu, Malaysia

[c] O. Eljamal
Water and Environmental Engineering Laboratory, Interdisciplinary Graduate School of Engineering Sciences, Kyushu University, 6-1 Kasuga-Koen Kasuga, Fukuoka 816-8580, Japan

[d] T. Mandai
Battery and Cell Materials Fields, Research Center for Energy and Environmental Materials (GREEN), National Institute for Materials Science (NIMS), 1-1 Namiki, Tsukuba, Ibaraki, 305-0044, Japan

Supporting information for this article is available on the WWW under https://doi.org/10.1002/batt.202400231

Research Article
doi.org/10.1002/batt.202400231
Chemistry Europe
European Chemical Societies Publishing

Mg^{2+} ions reversibly. For instance, Liang *et al.* showed that graphene-like MoS_2 cathode materials delivered an excellent specific capacity of 170 mAh g^{-1} with a capacity retention of 95% after 50 cycles.[19] Also, Liu *et al.* illustrated that graphene-like MoS_2 coated with carbon (MoS_2/C) achieved an initial specific capacity of nearly 220 mAh g^{-1} in RMBs.[20] Although the previous studies reported excellent electrochemical performance of MoS_2-based cathodes in RMBs (25–170 mAh g^{-1}) and Mg^{2+}/Li^+ hybrid-ion batteries (MLIBs) (125–1009 mAh g^{-1}), our recent mini-review highlighted that most of these studies used all phenyl complex (APC) electrolytes.[21] APC electrolytes are highly corrosive due to the chloride species and can damage cell casings and most conventional current collectors at high potentials.[22,23] On the other hand, magnesium-fluorinated alkoxyaluminate ($Mg[Al(HFIP)_4]_2$) is a chloride-free electrolyte that exhibited remarkable electrochemical activity in RMBs, low overpotentials (< 60 mV), high Coulombic efficacy (> 99%), and high anodic stability (3.8 V *vs.* Mg/Mg^{2+}).[24,25] Thus, for a step forward toward the realization of RMBs in practical applications, this research aims to investigate for the first time the compatibility of various MoS_2-based cathodes with $Mg[Al(HFIP)_4]_2$, as a promising electrolyte, in RMBs and MLIBs. The objectives of this study are as follows: (I) investigate the effect of hydro/solvothermal synthesis conditions on the electrochemical activity of MoS_2, (II) explore the electrochemical competence of heteroatom doped-MoS_2 in RMBs, (III) discuss the influence of graphene oxide incorporation on the electrochemical performance of MoS_2 in RMBs, and lastly (IV) examine the performance of MoS_2 in Mg^{2+}/Li^+ dual-salt electrolytes.

2. Materials and Methods

2.1. Materials

Section S2 in the supporting information summarizes the chemicals used in this research. All chemicals were of analytical grade and used as received without prior treatment. Also, all chemical solutions were prepared by using ultrapure water (UPW) (18.2 MΩ cm at 25 °C, Direct-Q® 3 UV, Merck Millipore).

2.2. Synthesis of Active Materials

2.2.1. MoS_2 Nanomaterials

MoS_2 was synthesized via the hydrothermal and solvothermal techniques. In the literature, there are a variety of synthesis protocols for MoS_2 in terms of Mo and S sources, Mo and S concentrations, solvent type, thermal temperature, thermal treatment time, and so on. Therefore, to recommend a synthesis procedure, seven different synthesis methods were carefully selected to produce MoS_2. The synthesis conditions of each method are summarized in Table 1. Method 1,[19] 2,[26] 3,[27] and 4[28] were chosen because their MoS_2 exhibited a good initial specific capacity as cathode materials in RMBs (i.e., > 100 mAh g^{-1}). On the other hand, methods 5,[17] 6,[29] and 7[30]

Table 1. Details of methods used to synthesize MoS_2 nanomaterials.

Method no.	Precursors and concentrations		Solvent	*T* (°C)	Time (h)	Mass yield (g)	Specific capacity in RMBs	Ref.
M1	Molybdenum (VI) oxide	Thioacetamide	12 mL pyridine	150	16	0.020	170 mA h g^{-1}	[19]
	0.036 g	1 mmol (0.07513 g)						
M2	Sodium molybdate dihydrate	Thiourea	60 mL UPW	180	24	0.095	130 mA h g^{-1}	[26]
	0.62 g	1.14 g						
M3	Ammonium molybdate tetrahydrate	Thioacetamide	40 mL UPW	190	12	1.036	100 mA h g^{-1}	[27]
	1.24 g	0.75 g						
M4	Ammonium molybdate tetrahydrate	Thiourea	60 mL UPW	200	18	0.827	–	[28]
	1.236 g	1.1989 g						
M5	Ammonium molybdate tetrahydrate	Thiourea	70 mL UPW	160	24	1.344	–	[17]
	2 mmol (2.472 g)	60 mmol (4.567 g)						
M6	Ammonium molybdate tetrahydrate	Thiourea	70 mL UPW	200	20	0.499	–	[29]
	0.6 g	1.2 g						
M7	Sodium molybdate dihydrate	Thiourea	30 mL UPW + 15 mL absolute ethanol	200	20	1.1	–	[30]

were selected because they were designed to produce MoS_2 with a high content of 1T-phase. The 1T-phase of MoS_2 is known to be metastable and more electronic conductive than the 2H-phase.[31,32] Hence, producing MoS_2 with high contents of 1T-phase is beneficial and may improve the electrochemical performance of MoS_2 as a cathode material.[33,34] The detailed procedures for synthesizing MoS_2 are summarized in section S3 in the supporting information. The produced MoS_2 materials via each method were denoted as M1, M2, M3, M4, M5, M6, and M7.

2.2.2. Heteroatom-Doped MoS_2 Nanomaterials

Heteroatom-doped MoS_2 nanomaterials namely, Mg–MoS_2, Cu–MoS_2, Co–MoS_2, Ni–MoS_2, Fe–MoS_2, Al–MoS_2, were synthesized following the procedures of method 5 (Table 1) except the addition of the dopant to the mixture of Mo and S precursors before the hydrothermal process. The molar ratio of (Mo:dopant) was selected as (30 : 1).

2.2.3. Graphene Oxide-Supported MoS_2 (GO-MoS_2)

Graphene oxide (GO) was prepared according to the Hummer method and following the steps reported by Idham *et al.*.[35] Previous articles mentioned that the incorporation of GO, after being thermally reduced at elevated temperatures (e. g., 800–1100 °C) under Ar or Ar/H_2 atmosphere for a specific period (e. g., 30–2 h), remarkably improved the electrochemical activity of MoS_2-based cathodes in RMBs.[33,34,36–39] However, the thermal reduction of GO increases the cost of rGO-MoS_2 and complicates its synthesis procedures. Hence, to reduce the cost of GO-MoS_2 production and simplify the synthesis process, GO without any treatment, was incorporated with MoS_2 in a one-step hydrothermal process according to the conditions of method 5 (Table 1). Detailed information on the synthesis of GO and GO-MoS_2 is provided in sections S4 and S5 in the supporting information.

2.3. Characterization of MoS_2 Nanomaterials

The external morphology of MoS_2 nanomaterials was revealed by scanning electron microscopy (SEM, SU8200, Hitachi, Japan). Moreover, the surface elemental composition of MoS_2 nanomaterials was obtained by energy dispersive spectroscopy (EDS, X-maxN, Horiba, Japan). X-ray diffraction analysis (XRD, SmartLab, Rigaku, Japan) was also performed to provide information about the crystalline structure of MoS_2 nanomaterials. The *d*-spacing and the crystallite size of MoS_2 nanomaterials were calculated using Bragg's and Scherrer's equations, respectively. In addition, X-ray photoelectron spectroscopy was conducted to analyze the valance state of elements on the surface of MoS_2 nanomaterials using the K-Alpha model from Thermo Fisher Scientific. Furthermore, the specific surface area of MoS_2 nanomaterials was measured using Quantachrome Nova 3200e. Before analysis, the samples were degassed for 4 h at 200 °C under vacuum. Then, N_2 adsorption/desorption isotherms were obtained at 77.3 K. The specific surface area of MoS_2 nanomaterials was estimated from N_2 adsorption/desorption isotherms using the theory of Brunauer-Emmett-Teller (BET).

2.4. Cathode Preparation and Electrochemical Measurements

The cathode materials were prepared by mixing MoS_2 nanomaterials with acetylene black and polyvinylidene fluoride (PVDF) by a mass ratio (wt%) of 80 : 10 : 10 in a proper amount of *N*-methyl-2-pyrrolidone (NMP, FUJIFILM Wako Pure Chemical Corporation, Japan).[40] The formed slurry was uniformly spread on a carbon-coated aluminum foil and dried in a vacuum oven at 80 °C for 24 h. Then, the cathode sheet was pressed (10.5 kN) and punched to provide a ∅16 mm cathode disc. The average mass density of the loaded materials was 2.50 mg cm^{-2}. Polished Mg foil, Whatman glass microfiber filter (GF/A, GE HealthCare, USA), and 0.3 M of $Mg[Al(HFIP)_4]_2$ dissolved in diethylene glycol dimethyl ether (G2; > 99.5 %, Kanto Chemical CO., INC., Japan) were used as an anode, separator, and electrolyte, respectively. The synthesis of $Mg[Al(HFIP)_4]_2$ powder is described elsewhere.[24] The battery cell was assembled in an argon-filled glovebox using a two-electrode cell. As a reference to the as-synthesized MoS_2 nanomaterials, a commercial MoS_2 (99 %, Kojundo Chemical Laboratory Co. Ltd, Japan) was also used to prepare a cathode material named C–MoS_2.

Galvanostatic discharge/charge experiments were conducted using a discharge/charge system (HJ1001SD8 C, HD Meiden Hokuto, Japan) at a voltage window of 0.3–3 V and 0.1–2 V *vs.* Mg^{2+}/Mg at room temperature (i. e., 25 °C). The cyclic voltammetry analysis (CV) was performed using an automatic polarization system (HSV-110, HD Meiden Hokuto, Japan) over a voltage range of 0.3–3 V and 0.1–2 V *vs.* Mg^{2+}/Mg at a scan rate of 1 mV s^{-1} *vs.* Mg^{2+}/Mg.

3. Results and Discussion

3.1. Characterization of MoS_2 Nanomaterials

The as-synthesized MoS_2 nanomaterials were characterized via different techniques to reveal their physicochemical properties. Liang *et al.*[19] and Wu *et al.*[26] reported in their articles that M1 and M2 exhibited excellent electrochemical performance as cathode materials in RMBs, i. e., 170 and 130 mAh g^{-1}, respectively. However, as shown in Table 1, the yield of these materials after the synthesis didn't exceed 100 mg which made the preparation of electrodes from these materials difficult. Therefore, M1 and M2 were excluded from the current research, and C–MoS_2, M3, M4, M5, M6, and M7 were only considered for further investigation and analysis.

The external morphology of MoS_2 nanomaterials was observed by SEM as displayed in Figure 1. Figure (1.a) manifests that C–MoS_2 was composed of several sheets stacked and layered in an irregular plate form. On the other hand, Figures

Research Article
doi.org/10.1002/batt.202400231
Chemistry Europe
European Chemical Societies Publishing

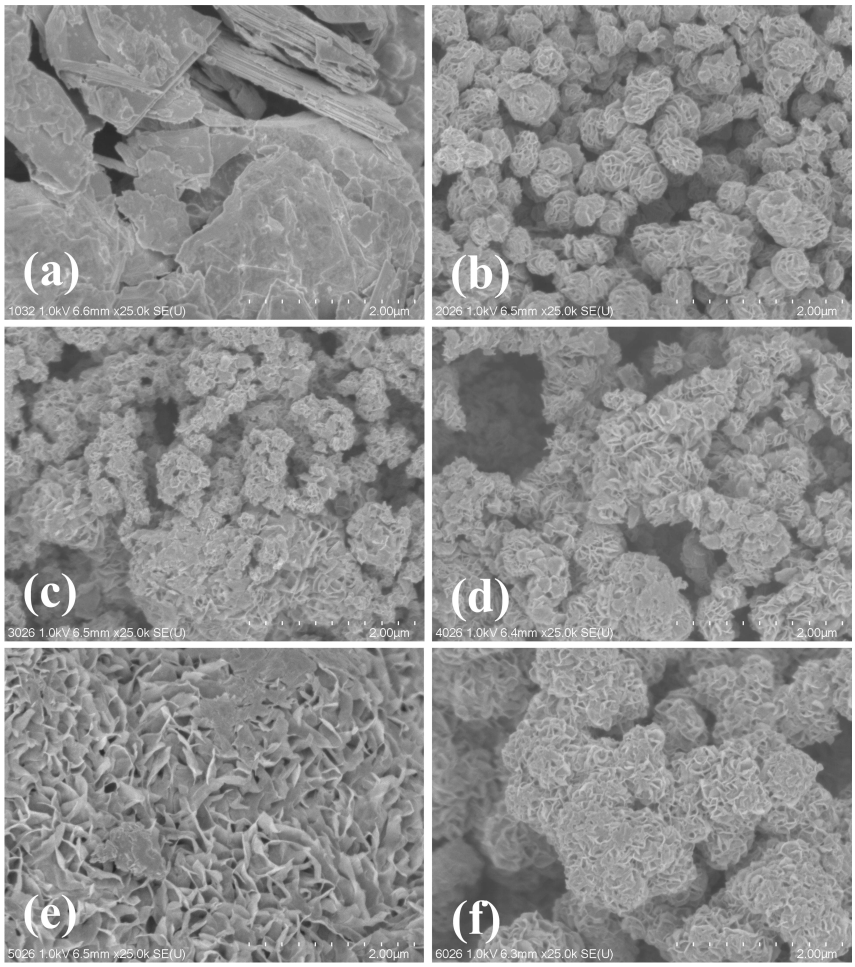

Figure 1. SEM observation of (a) C–MoS_2, (b) M3, (c) M4, (d) M5, (e) M6, and (f) M7.

(1.b)–(1.f) show that the as-synthesized M3, M4, M5, M6, and M7 consisted of thin sheets grown in a flower-like structure. Moreover, the EDS elemental mapping of all MoS_2, presented in Figure S1, demonstrates that both S and Mo were evenly distributed over the scanned area for all MoS_2 nanomaterials.

The crystallographic and phase structure of MoS_2 nanomaterials were identified via XRD analysis. The characteristic peaks of pure MoS_2 were identified in the XRD spectrum of C–MoS_2 as seen in Figure S2.[36,41,42] These strong and sharp peaks are indexed to the hexagonal 2H-phase of MoS_2. In addition, Table S2 illustrates that the *d*-spacing and crystallite size of C–MoS_2, calculated from the strong peak (002) at 14.34°, are 0.62 nm and 80.6 nm, respectively. This indicates that C–MoS_2 is highly crystalline and its layers are well-stacked along the *c-axis*.[20,34] On the other hand, the XRD patterns of the as-synthesized MoS_2 nanomaterials emphasize that each material had a distinctive phase structure (Figure 2). For instance, M3, M5, and M7 exhibited a 2H-phase structure. While M4 and M6 belong to the 3R-phase. Furthermore, Figure 2 illustrates that the XRD patterns of the as-synthesized MoS_2 nanomaterials consist of few broad and weak peaks. These broad peaks may result from the amorphous structure and the small crystallite size of the as-prepared MoS_2 nanomaterials (i.e., <10 nm) compared to the C–MoS_2 (i.e., ~80 nm) as presented in Table S2.[43] The weak and broad peaks in the XRD profiles of the as-synthesized MoS_2, particularly at the (002) plane, imply that these materials are highly exfoliated with a few layers stacked in the *c-axis*.[19,36] Furthermore, Table S2 demonstrates that the *d*-spacing of the as-prepared MoS_2 materials is slightly larger than that of C–MoS_2. The expansion of the *d*-spacing of the as-produced MoS_2 will promote the electrochemical performance of RMBs by reducing the energy barrier of Mg^{2+} intercalation/de-intercalation during the discharge/charge processes.[20,44]

XPS analysis was carried out to identify the chemical composition of MoS_2 nanomaterials. The full XPS spectra of MoS_2 nanomaterials are shown in Figure S3. It illustrates that all MoS_2 materials are mainly composed of Mo and S with trivial concentrations of O and C. The valance state of Mo and S is also investigated via XPS analysis and the high-resolution spectra of Mo 3d and S 2p for all MoS_2 materials are presented in Figure 3. Figure (3.a) demonstrates that the high-resolution spectra of Mo 3d for C–MoS_2 mainly consists of three distinctive peaks at binding energies of 232.28, 229.18, and 226.48 eV, which are assigned to $3d_{5/2}$ Mo^{4+}, $3d_{3/2}$ Mo^{4+}, and S 2 s, respectively.[45–47] On the contrary, the high-resolution spectra of Mo 3d for M3

Research Article
doi.org/10.1002/batt.202400231
Chemistry Europe
European Chemical Societies Publishing

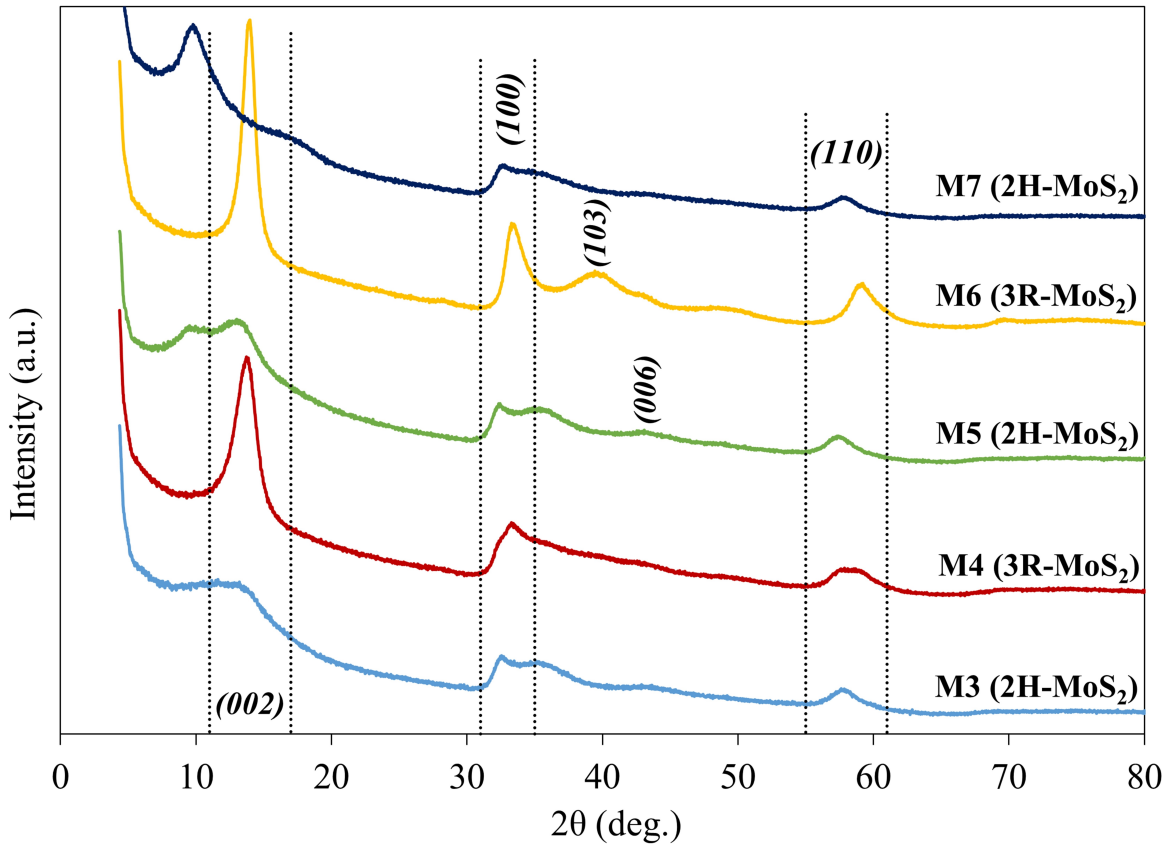

Figure 2. XRD patterns of the as-synthesized M3, M4, M5, M6, and M7.

[Figure (3.c)], M4 [Figure (3.e)], M5 [Figure (3.g)], M6 [Figure (3.i)], and M7 [Figure (3.k)] and Table S3 show that the characteristic peaks of Mo^{4+} ($3d_{5/2}$ and $3d_{3/2}$) shifted to lower binding energy due to the likelihood formation of the metallic 1T-phase of MoS_2 along with the 2H-phase.[48,49] For instance, Figure (3.g) proves that M5 consists of approximately 76% of the 1T-phase, represented by the evolution of the $3d_{5/2}$ Mo^{4+} and $3d_{3/2}$ Mo^{4+} of 1T–MoS_2 at a binding energy of 228.48 and 231.68 eV, respectively.[17,50] While the 2H-phase in M5 (24%) is evident from the emergence of the $3d_{5/2}$ Mo^{4+} of 2H-phase at a binding energy of 229.28 eV [Figure (3.g)].[17,50] Besides the oxidation state Mo^{4+}, the broad peaks of Mo 3d for the as-synthesized MoS_2 nanomaterials suggest that different oxidation states of Mo might exist.[51] For example, the high-resolution spectra of Mo 3d for M3 [Figure (3.c)], M5 [Figure (3.g)], and M7 [Figure (3.k)] manifest the evolution of two extra small peaks at 235.48 eV and 232.88 eV which are assigned to the $3d_{3/2}$ and $3d_{5/2}$ of Mo^{6+}, respectively.[46,52] The appearance of such peaks may arise from the possible oxidation of MoS_2 by air.[53]

Figure (3.b) describes the high-resolution scan of S 2p spectra for C–MoS_2 and it elucidates that the two peaks that emerged at 162.08 and 163.28 eV are corresponding to the $2p_{3/2}$ and $2p_{1/2}$ orbits of S^{2-}, respectively.[54] The same peaks were observed in the high-resolution spectra of S 2p for M3 [Figure (3.d)], M4 [Figure (3.f)], M5 [Figure (3.h)], M6 [Figure (3.j)], and M7 [Figure (3.l)] but at lower binding energy, as shown in Table S3, further supporting the formation of the 1T-phase of MoS_2.[48,55]

The BET surface area analysis of MoS_2 materials indicates that C–MoS_2 had a small BET-specific surface area (SSA_{BET}) of 3.11 $m^2 g^{-1}$ (Table S4) due to the micro-size of C–MoS_2 [Figure (1.a)]. On the contrary, Table S4 shows that some of the hydrothermally synthesized MoS_2 nanomaterials such as M3, M4, and M5 exhibited higher SSA_{BET} of 25.80, 20.44, and 25.73 $m^2 g^{-1}$, respectively. While the hydrothermally produced M6 and M7 exhibited trivial SSA_{BET} values of 0.24 and 0.30 $m^2 g^{-1}$, respectively (Table S4).

3.2. Electrochemical Performance of MoS_2-Based Cathodes in RMBs

The compatibility of various MoS_2-based cathodes with Mg[Al-(HFIP)$_4$]$_2$ electrolyte was evaluated using two-electrode battery cells. Figure 4 represents the galvanostatic discharge/charge curves of MoS_2-based cathodes in RMBs at a current density of 20 mA g^{-1} within a voltage window of 0.3–3 V at room temperature. Figure (4.a) illustrates that C–MoS_2 exhibited an initial discharge capacity of nearly 5.5 mAh g^{-1} and gradually decreased to approximately 3 mAh g^{-1} after 20 cycles. The poor performance of C–MoS_2 highlights the fact that Mg^{2+} can barely de/intercalate in a well-stacked and highly crystalline MoS_2 material due to a high energy barrier (i.e., 2.61 eV) caused

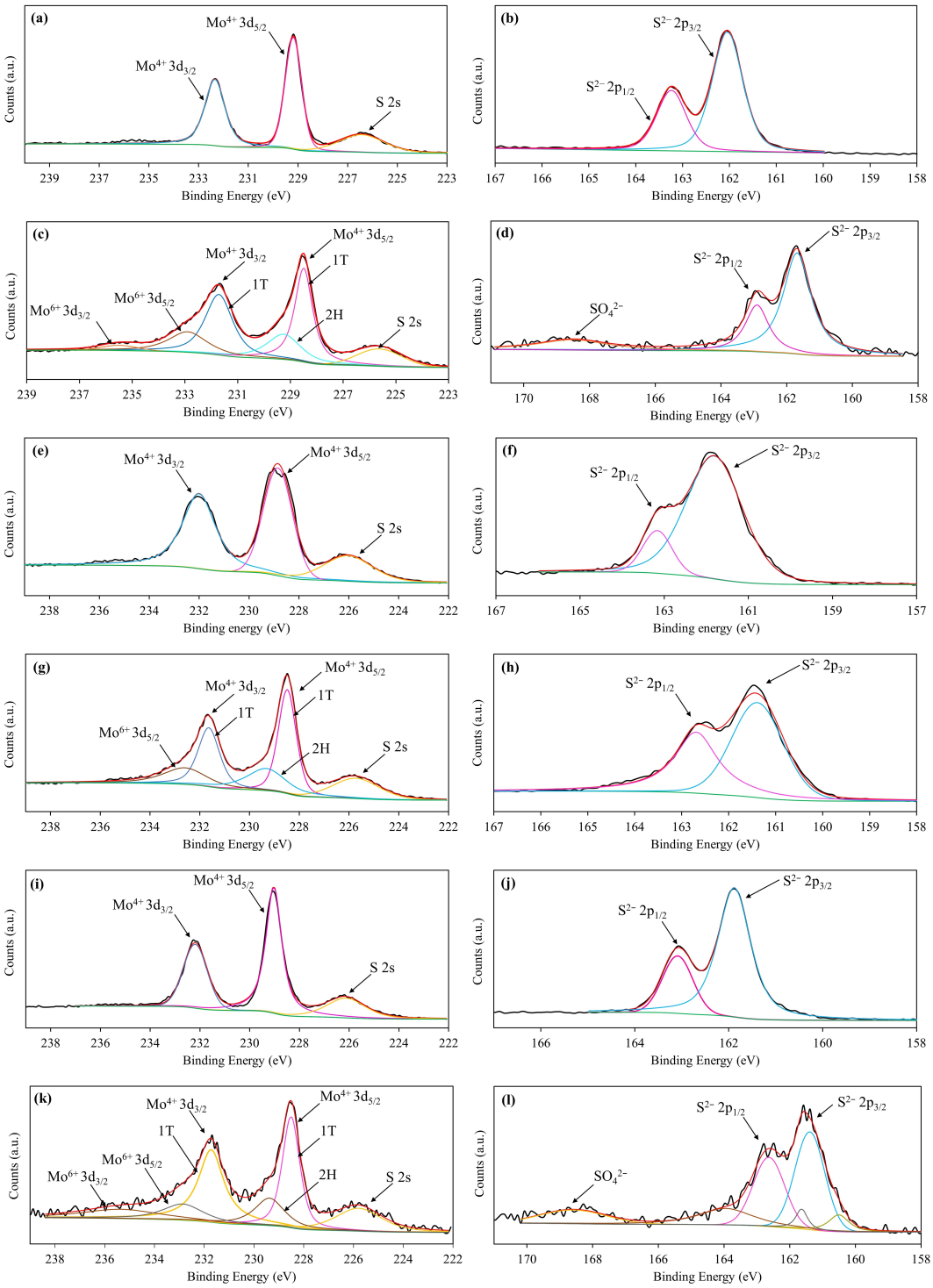

Figure 3. High-resolution XPS spectra of Mo 3d and S 2p for C–MoS_2 (a,b), M3 (c,d), M4 (e,f), M5 (g,h), M6 (i,j), and M7 (k,l).

by the large charge density of Mg^{2+} ions.[44,56,57] In addition, the low SSA_{BET} of C–MoS_2 (i.e., 3.11 $m^2 g^{-1}$) could limit the number of electrochemically active sites on the surface of C–MoS_2 which restricts the Mg^{2+} insertion/extraction reactions.[58,59]

On the other hand, Figures (4.b)–(4.f) elaborate that the electrochemical activity of the as-synthesized MoS_2 nanomaterials (e.g., M3, M4, M5, M6, and M7) significantly varied in RMBs. For instance, Figure (4.b) shows that M3 delivered an initial discharge capacity of 27 mAh g^{-1}. Nevertheless, M3 started to experience an overcharging state from the 3rd cycle until it reached its maximum in the 5th cycle (i.e., ~200 mAh g^{-1}) where the Coulombic efficiency abnormally increased to nearly 580% [Figure (S4.b)]. Likewise, M4 also exhibited irregular and overcharging reactions in the 10th and 20th cycles [Figure (4.c)]. Du

Research Article
doi.org/10.1002/batt.202400231
Chemistry Europe
European Chemical Societies Publishing

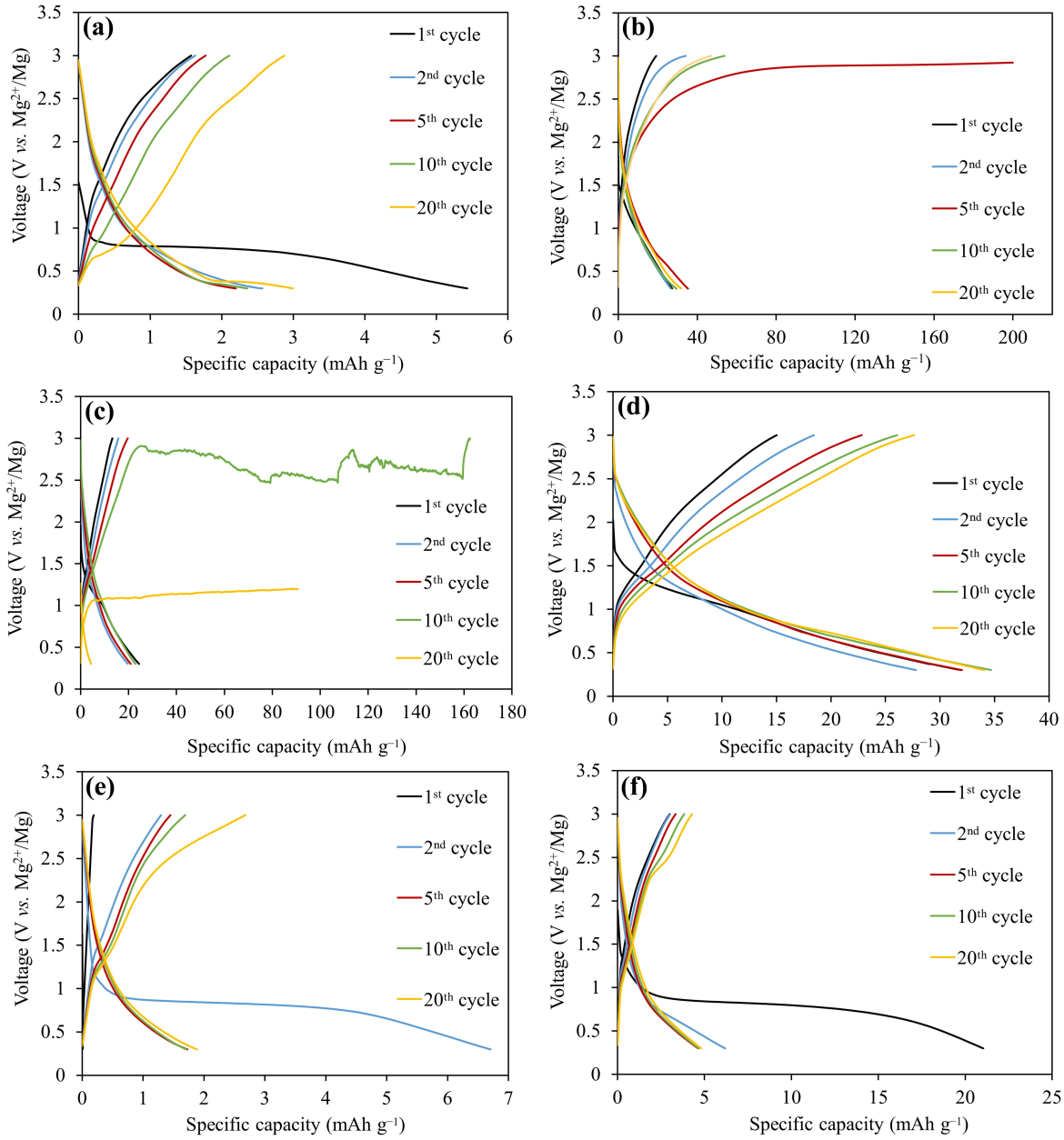

Figure 4. Galvanostatic discharge/charge curves of MoS_2-based cathode materials in RMBs at 20 mA g^{-1} and 25 °C. (a) C–MoS_2, (b) M3, (c) M4, (d) M5, (e) M6, and (f) M7.

et al. reported a similar overcharging behavior for the [Mg | 0.3 M $Mg(AlCl_2EtBu)_2$/THF | CuSe] cells.[56] The unstable charge voltages of M3 and M4 during cycling could be explained by the rapid degradation of the cathode material and the decomposition of the electrolyte during discharge in the first cycles.[60] Thus, the unstable overcharging phenomenon indicates that M3 and M4 are not compatible with $Mg[Al(HFIP)_4]_2$/G2 electrolytes at wide working voltages (e.g., 0.3–3 V). In comparison, M5 achieved an initial discharge capacity of 31 mAh g^{-1} through stable and reversible discharging/charging processes [Figure (4.d)]. The discharge capacity of M5 slightly increased to approximately 35 mAh g^{-1} after 20 cycles [Figure (S4.d)] and sustained for 40 cycles (Figure S5). It was previously mentioned that Lui *et al.* optimized the hydrothermal reaction of ammonium molybdate tetrahydrate and thiourea at 160 °C to produce M5 with a high content of 1T-phase (~70%) to facilitate the insertion of zinc ions (Zn^{2+}).[17]

With that being said, the high content of the metallic 1T-phase in M5 improves the electric conductivity of the cathode material and ensures a smooth transfer of electrons during the reversible intercalation/deintercalation of Mg^{2+} in RMBs. On the contrary, M6 and M7 exhibited a less attractive electrochemical performance with a discharge capacity of less than 5 mAh g^{-1} after 20 cycles [Figures (4.e) & (4.f)].

Among the as-synthesized MoS_2 nanomaterials, M3 was the only material used in RMBs. Liu *et al.* stated that M3 achieved a

specific capacity of 50 mAh g^{-1} at 100 mA g^{-1} and improved to nearly 100 mAh g^{-1} after 100 cycles.[27] Initially, it was assumed that the difference between the performance of M3 in both studies was due to the difference in electrolytes. Liu *et al.* used 0.4 M of APC electrolyte in their study which might play an important role in enhancing the electrochemical activity of M3 in RMBs. However, some articles showed that hydrothermally synthesized MoS_2 with 0.4 M APC electrolyte exhibited a specific capacity of less than 25 mAh g^{-1}.[62] Another difference that could affect the electrochemical performance of M3 was the anode side as Liu *et al.* used AZ31 Mg alloy instead of pure Mg foil. Thus, to study the effect of the anode side, a battery cell was fabricated using AZ31 Mg alloy as anode and M5, the best MoS_2 material, as a cathode. Figure S6 elucidates that the initial specific capacity of M5 decreased from 31 mAh g^{-1} [Figure (4.d)] to approximately 25 mAh g^{-1} after replacing the pure Mg foil with AZ31 Mg alloy. Consequently, the reason behind the difference in the electrochemical performance of M3 in the current study and the study of Liu *et al.* remains unclear.

Cyclic voltammetry analysis (CV) was conducted to describe the electrochemical reactions of the as-synthesized MoS_2 with $Mg[Al(HFIP)_4]_2$ in RMBs. Figure S7 summarizes the CV profiles for all MoS_2 materials within a voltage window of 0.3–3 V at a scanning rate of 1 mV s^{-1}. In the first cycle, C–MoS_2 exhibited weak current densities with only one single cathodic peak at 0.75 V [Figure (S7.a)]. The neglectable current densities indicate that Mg^{2+} ions can barely intercalate in the interlayer distance of C–MoS_2 due to the high energy barrier. In contrast, the required energy for Mg^{2+} adsorption is only 0.48 eV which suggests that the trivial discharge capacity of C–MoS_2 (i.e., 5.5 mAh g^{-1}, Figure (4.a)) might result from the adsorption of Mg^{2+} ions on the surface and the edges of C–MoS_2.[62] As the reversible reactions proceeded, the current densities of C–MoS_2 became weaker, but two small anodic peaks emerged at 0.72 V and 2.17 V in the 5th cycle. Also, Figure (S7.a) shows that the cathode peak in the 5th cycle became smaller and broader and shifted to a higher voltage of around 1 V. Similar CV profiles were obtained when M6 [Figure (S7.e)] and M7 [Figure (S7.f)] were used as cathode materials, further confirming the inadequacy and ineffectiveness of these materials in RMBs. Conversely, the CV profiles of M3 [Figure (S7.b)], M4 [Figure (S7.c)], and M5 [Figure (S7.d)] emphasize that the electrochemical reactions in RMBs substantially enhanced and the anodic and cathodic peaks can be easily recognized. For instance, a cathodic peak appeared at 1.04–1.1 V in the CV curves of M5 which was ascribed to the intercalation of Mg^{2+} ions into the lattice of M5 [Figure (S7.d)]. While the anodic peak of M5 was located near 1.36–1.42 V, corresponding to the deintercalation of Mg^{2+} ions from the lattice of M5 [Figure (S7.d)]. The strong current densities in the CV profiles of M5 clearly state that M5 is more compatible with $Mg[Al(HFIP)_4]_2$ than the other as-synthesized MoS_2 nanomaterials.

The outcomes of this section conclude that the conditions of the thermal synthesis of MoS_2 can greatly affect the electrochemical properties of MoS_2 nanomaterials in RMBs. Although M5 exhibited a good electrochemical performance compared to the other MoS_2 nanomaterials, its efficiency as a cathode material for RMBs is still far from the practical applications and different enhancement technologies such as heteroatom doping, graphene incorporation, and Mg^{+2}/Li^{+} dual-salt electrolytes were applied to promote the electrochemical performance of M5 in RMBs.

3.3. Electrochemical Performance of Heteroatom Doped-MoS_2 in RMBs

According to our recent mini-review,[21] heteroatom doping of MoS_2 is rarely applied to enhance the electrochemical performance of MoS_2 nanomaterials in RMBs. Therefore, this study would be the first to explore the influence of doping various elements, for example, Mg, Cu, Co, Ni, Fe, and Al, on the electrochemical performance of MoS_2 in RMBs.

Figure S8 shows that the XRD patterns of Mg–MoS_2, Cu–MoS_2, and Al–MoS_2 didn't significantly differ from the XRD pattern of M5 (Figure 2). On the other hand, new peaks have emerged in the XRD patterns of M5 after doping Co, Ni, and Fe which indicates that new phase structures of MoS_2 were formed (Figure S8). For example, the analysis of XRD data revealed that the phase structure of M5 has changed from 2H-phase (Figure 2) to 3R-phase because of doping Co and Ni. Although the phase structure of some doped-MoS_2 has changed after the doping process, Figure S8 manifests that the peak (002) for all doped-MoS_2 can still be observed at a diffraction angle (2θ) of 14.1° corresponding to an interlayer distance (*d*) of 0.63 nm. Since the interlayer distance of all doped-MoS_2 is close to that of M5 (Table S2), it indicates that the elements were deposited on the surface of M5 rather than being intercalated in the interlayer space of M5.

The as-synthesized doped-MoS_2 nanomaterials were used to prepare cathodes and tested as positive electrodes for RMBs. Figures 5 and S9 illustrate that all doped MoS_2-based cathodes exhibited initial capacities of less than 35 mAh g^{-1} which severely deteriorated to less than 10 mAh g^{-1} after 10 cycles (Figures 5 & S9). Meanwhile, M5 maintained a discharge capacity of 35 mAh g^{-1} for 40 cycles (Figure S5). One of the possible reasons for this performance is that the doping percentage was high enough to disturb and destroy the structure of the active materials during the discharge/charge processes. This was obvious when the doped-MoS_2 nanomaterials were initially tested at an expanded voltage window of 0.3–3 V where the electrodes experienced irregular charging reactions. For instance, Figure S10 indicates that when the doped-MoS_2 nanomaterials, namely Mg–MoS_2, Cu–MoS_2, Co–MoS_2, and Ni–MoS_2, were cycled at an operational voltage window of 0.3–3 V, all cells exhibited overcharging capacities more than 200 mAh g^{-1}. Hence, to avoid such unfavorable conditions, the voltage window was narrowed to 0.1–2 V. In contrast to these findings, Zhuo *et al.* disclosed that Cu doping improved the initial discharge capacity of MoS_2 from nearly 90 to 156 mAh g^{-1} (+73.33%) while using 0.25 M of $MgCl_2$ and $AlCl_3$ dissolved in DME as an electrolyte for RMBs.[63] However, neither the synthesis procedures of Cu–MoS_2 nor the doping percentage were mentioned in the article which made it

Research Article
doi.org/10.1002/batt.202400231
Chemistry Europe
European Chemical Societies Publishing

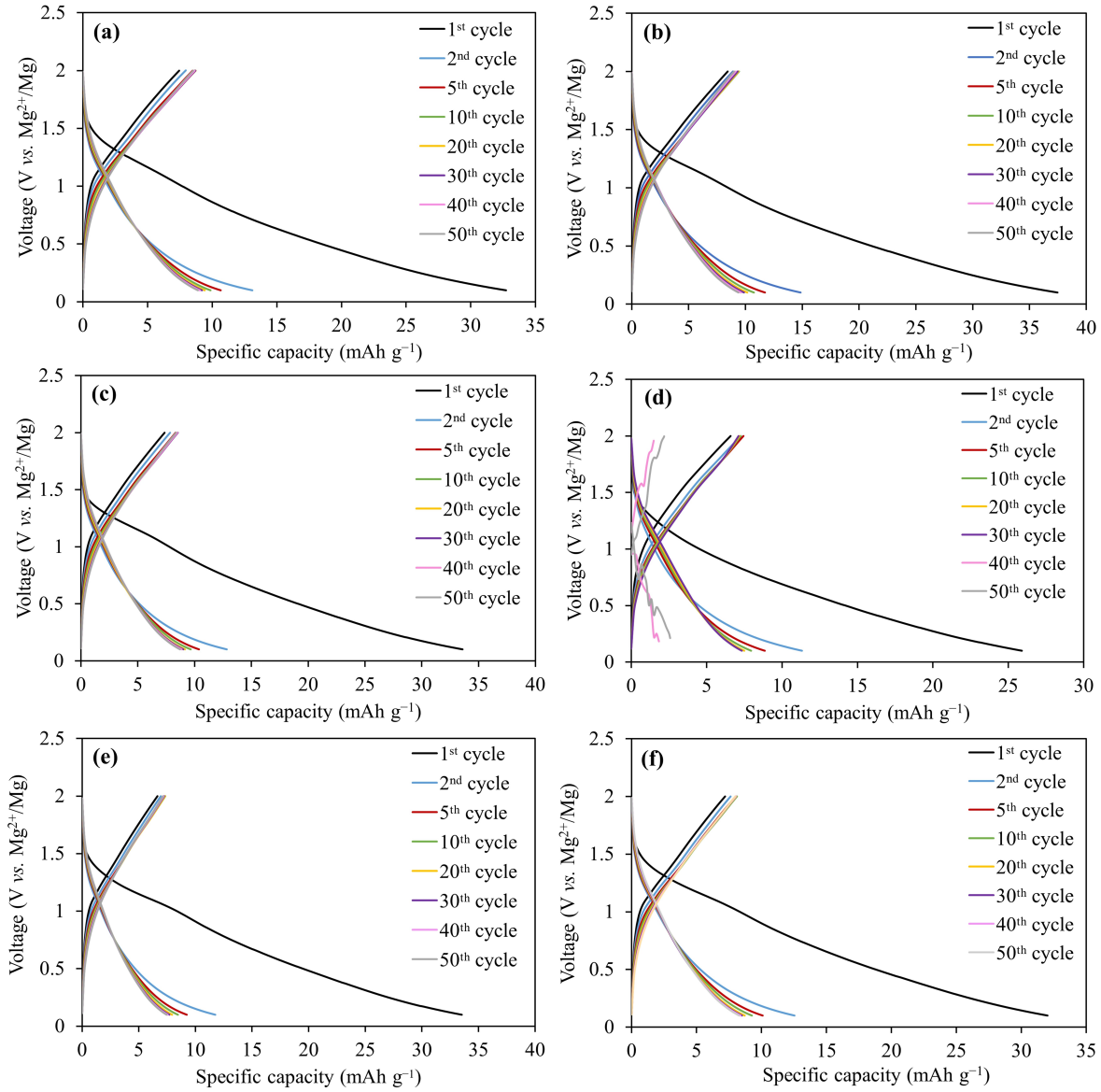

Figure 5. Galvanostatic discharge/charge curves of doped-MoS_2 nanomaterials in RMBs at 20 mA g^{-1} and 25 °C. (a) Mg–MoS_2, (b) Cu–MoS_2, (c) Co–MoS_2, (d) Ni–MoS_2, (e) Fe–MoS_2, and (f) Al–MoS_2.

difficult to compare and discuss their results with the current findings.

3.4. Electrochemical Performance of GO-MoS_2 in RMBs

Graphene is a 2D carbonaceous material with unique physical, chemical, and mechanical properties.[64] It stands out as a perfect substrate to grow MoS_2 in a one-pot hydrothermal process, preventing them from aggregating and promoting the electric conductivity of the electrode to facilitate the intercalation/deintercalation of Mg^{2+} ions in/from the lattice of MoS_2 nanomaterials.[36,37]

GO-MoS_2 heterostructure was synthesized in a one-pot hydrothermal process and was evaluated as a cathode material in RMBs. Figure (6.a) shows that the phase structure of GO-MoS_2 didn't significantly differ from the phase structure of M5 (Figure 2). More importantly, Figure (6.a) confirms that the interlayer distance of M5 at the (002) plane didn't expand after the incorporation of GO with M5 (*d*-spacing of GO-MoS_2 = 0.65 nm). Hence, it can be said that GO didn't intercalate between the layers of M5, but it was used as a flexible network to grow MoS_2 and improve its electrochemical properties. Figure (6.b) represents the SEM image of GO-MoS_2. It states that GO-MoS_2 retained the external shape of M5 [Figure (1.d)], and no substantial changes were observed in the morphology of GO-MoS_2 after the incorporation of GO. Figures (6.c) and (6.d) display the galvanostatic discharge/charge and cycling performance of GO-MoS_2 in RMBs at 20 mA g^{-1}. As a cathode material, GO-MoS_2 initially achieved a discharge capacity of 42.5 mAh g^{-1}, slightly better than M5 (35 mhA g^{-1}, Figure (4.d)). However, the discharge capacity of GO-MoS_2 dramatically dropped to less

Research Article
doi.org/10.1002/batt.202400231
Chemistry Europe
European Chemical Societies Publishing

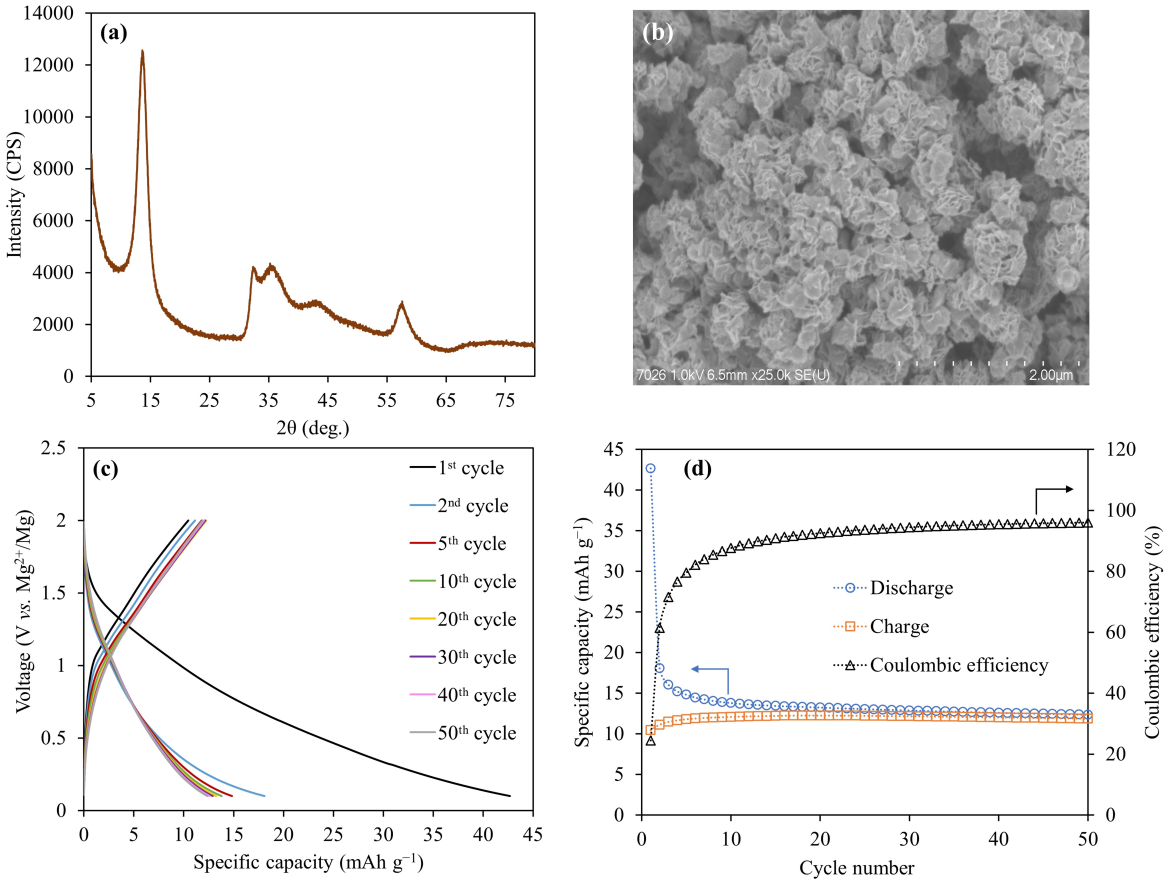

Figure 6. Characterization and electrochemical performance of GO-MoS_2 in RMBs at 20 mA g^{-1} and 25 °C. (a) XRD pattern of GO-MoS_2, (b) SEM image of GO-MoS_2, (c) galvanostatic discharge/charge curves, and (d) cycling performance of GO-MoS_2.

than 20 mAh g^{-1} and continued to decrease until it stabilized at less than 15 mAh g^{-1} after 50 cycles [Figure (6.d)]. This behavior indicates that GO neither expanded the interlayer distance nor enhanced the electric conductivity of the electrode which resulted in the fading of the discharge capacity immediately after the second cycle [Figure (6.d)].[19] These findings highlight the importance of reducing GO before the integration with MoS_2 in order to improve the electric conductivity of GO and ultimately promote the electrochemical performance of GO-MoS_2 heterostructures in RMBs.

3.5. Electrochemical Performance of MoS_2 in Mg^{2+}/Li^+ Dual-Salt Electrolyte (MLIBs)

Despite the similarity in the ionic radius (Table S1), the monovalent nature of Li^+ ions and the small activation energy (0.49 eV for Li^+ *vs.* 2.61 eV for Mg^{2+}) ensure the fast diffusion of Li^+ ions not only in MoS_2 but in a broad range of intercalation cathode materials.[38,62] Hence, to combine the benefit of using the free-dendrite Mg anode and the easy-intercalated Li^+ ions, many researchers have used the dual-salt electrolyte approach to facilitate either the solo intercalation of Li^+ ions (Daniell battery) or the simultaneous intercalation of Li^+ and Mg^{2+} ions (Rocking-chair battery) in the lattice of MoS_2 and promote the electrochemical reactions of RMBs.[21]

In this study, the influence of dual-salt electrolytes on the electrochemical performance of M5 was elaborated. Initially, a chloride-free Li^+ source such as Li[B(HFIP)$_4$] was selected to prepare the dual-salt electrolyte as follows: 0.4 M of Li[B(HFIP)$_4$] was dissolved with 0.2 M of Mg[Al(HFIP)$_4$]$_2$ in G2 for 24 h inside a glovebox and under the protection of argon gas.[65] Figure S11 shows that M5 experienced an irregular discharge voltage profile in the first cycle when the dual-salt electrolyte [0.2 M Mg[Al(HFIP)$_4$]$_2$/0.4 M Li[B(HFIP)$_4$]/G2] was used. However, the discharge/charge voltage profiles stabilized in the second and fifth cycles where the M5 exhibited improved discharge capacities of 89.66 and 77.33 mAh g^{-1}, respectively. Unfortunately, as the cycling proceeded and in the 10th cycle, the specific discharge capacity notably faded to less than 22 mAh g^{-1} and the cell experienced an abnormal overcharging process. This is probably due to the acceleration of the degradation of the cathode material and/or the electrolyte by the addition of Li[B(HFIP)] which confirms the incompatibility of Li[B(HFIP)$_4$, as a source of Li^+ ions, with Mg[Al(HFIP)$_4$]$_2$ in MLIBs.

The majority of the previous articles utilized lithium chloride (LiCl) as a source of Li^+ ions to improve the electrochemical performance of MoS_2 in APC electrolytes.[21] For example, Yu *et al.* showed that adding 1 M of lithium chloride (LiCl) to the

Research Article
doi.org/10.1002/batt.202400231
Chemistry Europe
European Chemical Societies Publishing

APC electrolyte improved the electrochemical performance of the anion-rich MoSSe/G from 76.9 mAh g^{-1} (APC) to 299.2 mAh g^{-1} (APC/LiCl) after 400 cycles.[66] Also, Li *et al.* elucidated that adding 0.8 M of LiCl to the APC electrolyte was enough to shorten the activation time of pristine MoS_2 from 190 to 50 cycles and approximately doubled the specific capacity after 300 cycles.[47] Hene, LiCl was used to prepare another set of dual-salt electrolytes. Different concentrations of LiCl, e.g., 0.1, 0.2, and 0.3 M and 0.3 M of $Mg[Al(HFIP)_4]_2$ were dissolved in G2 under the protection of argon gas for 24 h. LiCl concentration couldn't be increased more than 0.3 M due to the solubility limit of LiCl in G2. Figure 7 presents the galvanostatic discharge/charge curves and cycling performance of M5 using the prepared dual-salt electrolytes. It is evident from Figure 7 that the addition of LiCl had a positive effect on the electrochemical activity of M5. For example, Figure 7 shows that adding 0.1. 0.2, and 0.3 M of LiCl remarkably improved the initial discharge capacity of M5 from 31 to approximately 80 [Figure (7.a)], 90 [Figure (7.b)], and 106 mAh g^{-1} [Figure (7.c)], respectively. Furthermore, it can be noticed from Figure 7 that the voltage difference between the charge and discharge curves reduced as the concentration of LiCl increased from 0.1 to 0.3 M which indicates that the polarization significantly decreased.[67]

The role of Li^+ and Cl^- ions in the enhancement of the electrochemical activity of M5 in MLIBs was distinguished by adding 0.1 M of $MgCl_2$, as another source of Cl^-, to 0.3 M of $Mg[Al(HFIP)_4]_2$ and used as an electrolyte to prepare the battery cell. Figure S12 illustrates that the galvanostatic discharge/charge curves didn't change after the addition of 0.1 M of $MgCl_2$. This points out that Cl^- ions had a negligible effect on improving the performance of M5 in MLIBs. Thus, it can be said that the electrochemical improvements in Figure 7 mainly resulted from the presence of the highly active Li^+ ions in the electrolyte. Inductively coupled plasma optical emission spectroscopy analysis (5800 ICP-OES, Agilent) was performed to confirm the simultaneous insertion of Mg^{2+} and Li^+ ions in the lattice of M5. Figure S13 summarizes the results of ICP-OES analysis for M5 in single and dual-salt electrolytes. The presented concentrations of Mg and Li in Figure S13 are normalized with respect to the number of Mo moles. Figure S13 demonstrates that 0.065 of Mg was intercalated into the lattice of M5 after being discharged to 0.1 V in $Mg[Al(HFIP)_4]_2$/G2 electrolyte. On the other hand, the proportion of Mg^{2+} intercalated in the lattice of M5 was increased to 0.12 along with 0.51 of Li^+ after the discharge of the cell to 0.1 V in the dual-salt electrolyte [0.3 M $Mg[Al(HFIP)_4]_2$/0.3 M LiCl/G2]. The simultaneous insertion of Mg^{2+} and Li^+ ions emphasizes that the fabricated cell is a rocking-chair cell where the preferentially intercalated Li^+ ions were responsible for accelerating the insertion of the divalent Mg^{2+} ions and improving the electrochemical activity of MoS_2 nanomaterials in MLIBs. At low potentials, Li^+ ions are pre-intercalating in the lattice of M5 because of the low activation energy (i.e., 0.49 V), disordering the layered structure of M5, and creating faster routes with lower activation energies that facilitated the intercalation of

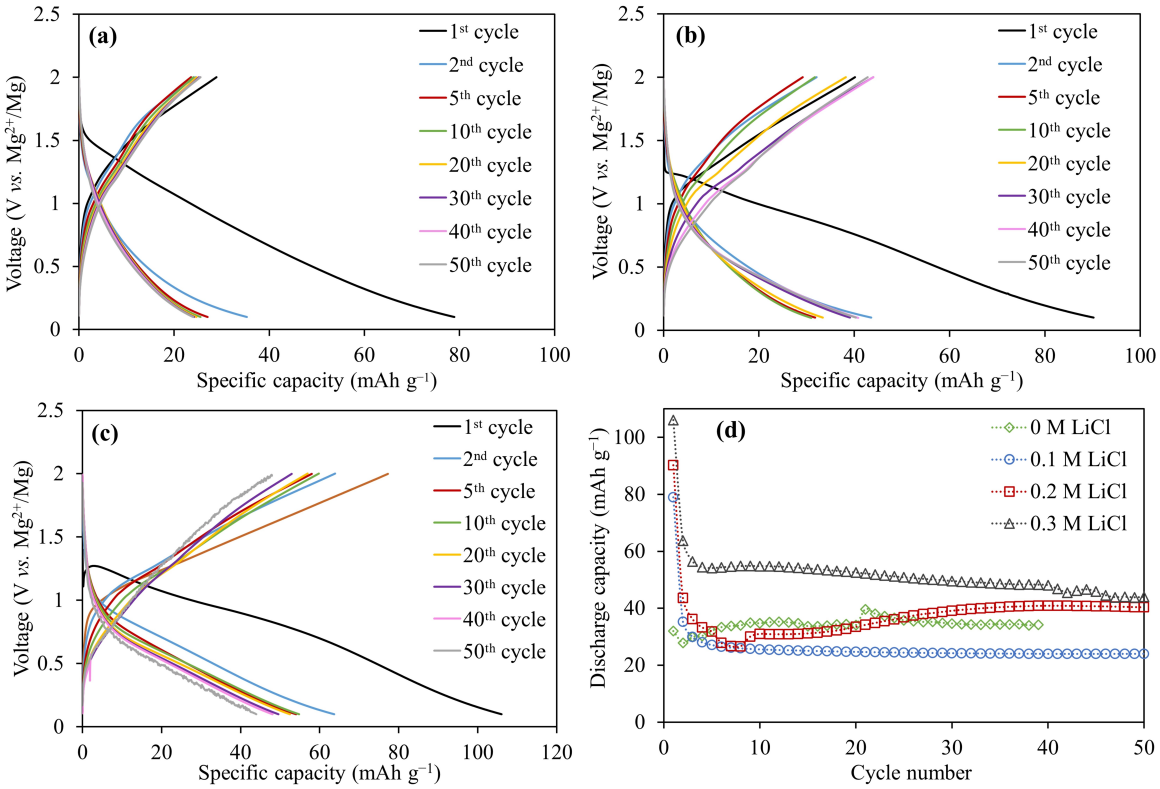

Figure 7. Galvanostatic discharge/charge curves of M5 in MLIBs at 20 mA g^{-1} and 25 °C. (a) 0.1 M LiCl, (b) 0.2 M LiCl, (c) 0.3 M LiCl, and (d) cycling performance of M5.

Mg^{2+} ions and enhanced the specific capacity of M5 in MLIBs.[38,47,68] In addition, the intercalation of Li^+ ions could be accompanied by a phase transformation of MoS_2 from the 2H-phase to the 1T-phase which ensured a faster electron transfer during the intercalation of Mg^{2+}.[34,69]

However, Figure 7 demonstrated that at all concentrations of LiCl, the initial discharge capacity of M5 decreased in the second cycle by approximately 50%. As the cycling proceeded, the specific capacity of M5 gradually stabilized and 55% (0.1 M LiCl), 63% (0.2 M LiCl), and 41% (0.3 M LiCl) of the initial capacity were attained after 50 cycles [Figure (7.d)]. The outcomes of ICP-OES state that 25% of the intercalated Mg^{2+} ions (i.e., 0.03 out of 0.12) and less than 51% of Li^+ ions (i.e., 0.26 out of 0.51) were extracted from M5 in the first charge cycle (Figure S13). The proportion of the deintercalated Mg^{2+} ions further decreased to 20% in the second charge cycle, whereas the percentage of the extracted Li^+ ions increased to nearly 60% (Figure S13). These findings point out that the sluggish extraction of Mg^{2+} ions and the partial entrapment of Li^+ ions could be responsible for the rapid decrease in the specific capacity of M5 in MLIBs.[38,66] A similar rapid decrease in the initial discharge capacity was also reported by Yu *et al.*[38] and Fan *et al.*[68] when they used MoS_2/G and SnS_2–MoS_2, respectively, as cathode materials in (APC/LiCl) dual-salt electrolytes.

The nature of the electrochemical reaction of M5 with the dual-salt electrolytes was further clarified by carrying out the CV analysis. Figure S14 shows that the current density of the CV curves gradually increased as the concentration of LiCl increased in the dual-salt electrolytes. This indicates that the electrochemical reactions were boosted by the addition of LiCl to $Mg[Al(HFIP)_4]_2$. Figure S14 also demonstrates that the cathodic peak (~1 V) and anodic peak (~1.36 V) of M5 in $Mg[Al(HFIP)_4]_2$ [Figure (S7.d)] notably weakened by the addition of 0.1 M of LiCl. However, they became more pronounced after increasing LiCl concentration to 0.2 and 0.3 M. These redox peaks are ascribed to the intercalation and deintercalation of Mg^{2+} and Li^+ in a reversible manner.[28,69]

4. Conclusions

This study investigates for the first time the electrochemical activity of various MoS_2 nanomaterials in fluorinated alkoxyaluminate electrolytes ($Mg[Al(HFIP)_4]_2$). Seven MoS_2 nanomaterials, namely M1, M2, M3, M4, M5, M6, and M7, were synthesized via different solvothermal and hydrothermal techniques and tested as a positive electrode in RMBs. Among the as-synthesized MoS_2, M5 exhibited superb electrochemical activity in RMBs by delivering a specific capacity of 35 $mAh\,g^{-1}$ over 40 cycles. This excellent performance was ascribed to the high content of the metallic 1T-phase in M5 (~70%). Furthermore, M5 was modified by heteroatom doping, graphene oxide incorporation, and dual-salt electrolyte to improve its electrochemical performance in RMBs. The results showed that all doped-MoS_2 exhibited unsatisfactory performance in RMBs (< 35 $mAh\,g^{-1}$). This poor performance might result from the high doping percentage (Mo:dopant = 30:1) that disturbed the structure of the active material and impaired its electrochemical activity in RMBs. Similarly, graphene oxide incorporation didn't improve the electrochemical performance of M5 in RMBs. On the contrary, the dual-salt electrolytes ($Mg[Al(HFIP)_4]_2$/LiCl) remarkably boosted the electrochemical activity of M5 in MLIBs. The addition of 0.1, 0.2, and 0.3 M of LiCl to 0.3 M of $Mg[Al(HFIP)_4]_2$ promoted the initial specific capacity from 31 to 80, 90, and 106 $mAh\,g^{-1}$, respectively. This is due to the presence of the highly active Li^+ ions in the electrolyte which played a vital role in accelerating the charge transfer, reducing the diffusion energy barrier, and ultimately boosting the electrochemical performance of M5 in MLIBs. However, the electrochemical enhancement of M5 in MLIBs was hampered by the solubility limit of LiCl in G2. Therefore, to further promote the electrochemical performance of M5, it is recommended to explore other Li^+ sources with high solubility in G2.

Acknowledgements

This research was supported by the NEXT Center of Innovation Program (COI-NEXT) and GteX Program of the Japan Science and Technology Agency with grant number JPMJPF2016 and JPMJGX23S1, respectively, and by the MEXT Promotion of Distinctive Joint Usage/Research Center Support Program with grant number JPMXP0723833161. T.M. also thanks the financial support by KAKENHI with grant number JP21K05263 of the Japan Society for the Promotion of Science. Additionally, the authors express their gratitude to Dr. UPM Ashik from Kyushu University for his valuable assistance in conducting the surface area analysis for MoS_2 nanomaterials.

Conflict of Interests

The authors declare no conflict of interest.

Data Availability Statement

The data that support the findings of this study are available from the corresponding author upon reasonable request.

Keywords: MoS_2 · $Mg[Al(HFIP)_4]_2$ · Heteroatom doping · Graphene oxide-MoS_2 heterostructure · Li^+/Mg^{2+} dual-salt electrolytes

[1] A. Manthiram, *ACS Cent. Sci.* **2017**, *3*, 1063–1069.
[2] S. Chen, S. Fan, H. Li, Y. Shi, H. Y. Yang, *Coord. Chem. Rev.* **2022**, *466*, 214597.
[3] M. Kotobuki, B. Yan, L. Lu, *Energy Storage Mater.* **2023**, *54*, 227–253.
[4] X. Lin, J. Liu, H. Zhang, Y. Zhong, M. Zhu, T. Zhou, X. Qiao, H. Zhang, T. Han, J. Li, *Adv. Sci.* **2021**, *8*, 2002298.
[5] S. Yang, D. Li, T. Zhang, Z. Tao, J. Chen, *J. Phys. Chem. C* **2012**, *116*, 1307–1312.
[6] Y. Shen, Q. Zhang, Y. Wang, L. Gu, X. Zhao, X. Shen, *Adv. Mater.* **2021**, *33*, 2103881.
[7] Y. Zhang, T. Li, S. Cao, W. Luo, F. Xu, *Chem. Eng. J.* **2020**, *387*, 124125.

[8] T. Mandai, K. Tatesaka, K. Soh, H. Masu, A. Choudhary, Y. Tateyama, R. Ise, H. Imai, T. Takeguchi, K. Kanamura, *Phys. Chem. Chem. Phys.* **2019**, *21*, 12100–12111.
[9] N. Yacout, H. S. Refai, M. A. Kebede, F. Salman, E. Sheha, *Mater. Chem. Phys.* **2022**, *292*, 126770.
[10] Z. Li, X. Mu, Z. Zhao-Karger, T. Diemant, R. J. Behm, C. Kübel, M. Fichtner, *Nat. Commun.* **2018**, *9*, 5115.
[11] Y. Shen, Y. Wang, Y. Miao, Q. Li, X. Zhao, X. Shen, *Adv. Mater.* **2023**, *35*, 2208289.
[12] D. Aurbach, Z. Lu, A. Schechter, Y. Gofer, H. Gizbar, R. Turgeman, Y. Cohen, M. Moshkovich, E. Levi, *Nature* **2000**, *407*, 724–727.
[13] Z. Li, I. Sami, J. Yang, J. Li, R. V. Kumar, M. Chhowalla, *Nat. Energy* **2023**, *8*, 84–93.
[14] S. Mateti, M. M. Rahman, P. Cizek, Y. Chen, *RSC Adv.* **2020**, *10*, 12754–12758.
[15] C. He, W. Yin, X. Li, J. Zheng, B. Tang, Y. Rui, *Electrochim. Acta* **2021**, *365*, 137353.
[16] M. L. Meyerson, P. E. Papa, J. A. Weeks, A. G. Paul-Orecchio, A. Heller, C. B. Mullins, *ACS Appl. Energ. Mater.* **2020**, *3*, 6121–6126.
[17] J. Liu, P. Xu, J. Liang, H. Liu, W. Peng, Y. Li, F. Zhang, X. Fan, *Chem. Eng. J.* **2020**, *389*, 124405.
[18] W. Xu, C. Sun, K. Zhao, X. Cheng, S. Rawal, Y. Xu, Y. Wang, *Energy Storage Mater.* **2019**, *16*, 527–534.
[19] Y. Liang, R. Feng, S. Yang, H. Ma, J. Liang, J. Chen, *Adv. Mater.* **2011**, *23*, 640–643.
[20] Y. Liu, L. Jiao, Q. Wu, J. Du, Y. Zhao, Y. Si, Y. Wang, H. Yuan, *J. Mater. Chem. A* **2013**, *1*, 5822–5826.
[21] O. Falyouna, T. Mandai, *Proc. Int. Exch. Innov. Conf. Eng. Sci.* **2023**, *9*, 34–42.
[22] L. Wang, B. Jiang, P. E. Vullum, A. M. Svensson, A. Erbe, S. M. Selbach, H. Xu, F. Vullum-Bruer, *ACS Nano* **2018**, *12*, 2998–3009.
[23] T. Pavčnik, M. Lozinšek, K. Pirnat, A. Vizintin, T. Mandai, D. Aurbach, R. Dominko, J. Bitenc, *ACS Appl. Mater. Interfaces* **2022**, *14*, 26766–26774.
[24] T. Mandai, Y. Youn, Y. Tateyama, *Mater Adv* **2021**, *2*, 6283–6296.
[25] T. Pavčnik, J. Imperl, M. Kolar, R. Dominko, J. Bitenc, *J. Mater. Chem. A* **2024**, *12*, 3386–3397.
[26] C. Wu, G. Zhao, S. Gong, N. Zhang, K. Sun, *J. Mater. Chem. A* **2019**, *7*, 4426–4430.
[27] J. Liu, Y. Zhong, X. Li, T. Ying, T. Han, J. Li, *Nanoscale Adv.* **2021**, *3*, 5576–5580.
[28] Z. Xiong, G. Zhu, H. Wu, G. Shi, P. Xu, H. Yi, Y. Mao, B. Wang, X. Yu, *ACS Appl. Energ. Mater.* **2022**, *5*, 6274–6281.
[29] X. Zhou, D. Wu, Z. Jin, X. Song, X. Wang, S. L. Suib, *J. Mater. Sci.* **2020**, *55*, 16374–16384.
[30] B. Yu, Y. Chen, Z. Wang, D. Chen, X. Wang, W. Zhang, J. He, W. He, *J. Power Sources* **2020**, *447*, 227364.
[31] V. P. Hoang Huy, Y. N. Ahn, J. Hur, *Nanomaterials* **2021**, *11*, 1517.
[32] S. Das, G. Swain, K. Parida, *Mater. Chem. Front.* **2021**, *5*, 2143–2172.
[33] C.-J. Hsu, C.-Y. Chou, C.-H. Yang, T.-C. Lee, J.-K. Chang, *Chem. Commun.* **2016**, *52*, 1701–1704.
[34] X. Fan, R. R. Gaddam, N. A. Kumar, X. S. Zhao, *Adv. Energy Mater.* **2017**, *7*, 1700317.
[35] M. F. Idham, O. Falyouna, R. Eljamal, I. Maamoun, O. Eljamal, *J. Water Proc. Eng.* **2022**, *50*, 103289.
[36] Y. Liu, L.-Z. Fan, L. Jiao, *J. Power Sources* **2017**, *340*, 104–110.
[37] Y. Liu, L. Jiao, Q. Wu, Y. Zhao, K. Cao, H. Liu, Y. Wang, H. Yuan, *Nanoscale* **2013**, *5*, 9562–9567.
[38] X. Yu, G. Zhao, H. Huang, C. Liu, P. Lyu, N. Zhang, *Chem. Eng. J.* **2022**, *428*, 131214.
[39] C. Wu, G. Zhao, X. Yu, C. Liu, P. Lyu, G. Maurin, S. Le, K. Sun, N. Zhang, *Chem. Eng. J.* **2021**, *412*, 128736.
[40] Y. Tan, F. Zhou, Z. Huang, W. Yao, T. Zhang, H. Yao, L. Lu, S. Yu, *ChemElectroChem* **2018**, *5*, 996–1001.
[41] G. Venkateswarlu, D. Madhu, J. V. Rani, *Funct. Mater. Lett.* **2019**, *12*, 1950041.
[42] S. Wang, J. Zhang, D. He, Y. Zhang, L. Wang, H. Xu, X. Wen, H. Ge, Y. Zhao, *J. Phys. Chem. Solids* **2014**, *75*, 100–104.
[43] X.-L. Li, Y.-D. Li, *J. Phys. Chem. B* **2004**, *108*, 13893–13900.
[44] Y. Liang, H. D. Yoo, Y. Li, J. Shuai, H. A. Calderon, F. C. Robles Hernandez, L. C. Grabow, Y. Yao, *Nano Lett.* **2015**, *15*, 2194–2202.
[45] S.-J. Lee, Y.-S. Son, J.-H. Choi, S.-S. Kim, S.-Y. Park, *Catalysts* **2021**, *11*, 1229.
[46] W. Gu, Y. Yan, C. Zhang, C. Ding, Y. Xian, *ACS Appl. Mater. Interfaces* **2016**, *8*, 11272–11279.
[47] B. Li, Z. Li, H. Chen, X. Zhang, S. Wu, H. Xu, Y. Yao, Y. Li, X. Li, Z. Hu, *Mater. Today Energy* **2022**, *27*, 101047.
[48] Y. Li, K. Chang, Z. Sun, E. Shangguan, H. Tang, B. Li, J. Sun, Z. Chang, *ACS Appl. Energ. Mater.* **2019**, *3*, 998–1009.
[49] H. Liu, R. Wu, H. Zhang, M. Ma, *ChemCatChem* **2020**, *12*, 893–902.
[50] D. M. Sim, H. J. Han, S. Yim, M.-J. Choi, J. Jeon, Y. S. Jung, *ACS Omega* **2017**, *2*, 4678–4687.
[51] M. Manuja, V. Sarath Krishnan, G. Jose, in *IOP Conf. Ser. Mater. Sci. Eng.*, IOP Publishing, **2018**, p. 12015.
[52] X. Qiao, F. Hu, D. Hou, D. Li, *Mater. Lett.* **2016**, *169*, 241–245.
[53] S. Xu, Q. Zhu, T. Chen, W. Chen, J. Ye, J. Huang, *Mater. Chem. Phys.* **2018**, *219*, 399–410.
[54] B. Gao, X. Du, Y. Li, S. Ding, C. Xiao, Z. Song, *ACS Appl. Mater. Interfaces* **2019**, *12*, 877–885.
[55] R. Kappera, D. Voiry, S. E. Yalcin, B. Branch, G. Gupta, A. D. Mohite, M. Chhowalla, *Nat. Mater.* **2014**, *13*, 1128–1134.
[56] C. Du, W. Younas, Z. Wang, X. Yang, E. Meng, L. Wang, J. Huang, X. Ma, Y. Zhu, C. Cao, *J. Mater. Chem. A* **2021**, *9*, 3648–3656.
[57] P. Saha, M. K. Datta, O. I. Velikokhatnyi, A. Manivannan, D. Alman, P. N. Kumta, *Prog. Mater. Sci.* **2014**, *66*, 1–86.
[58] T. Mandai, A. Kutsuma, M. Konya, Y. Nakabayashi, K. Kanamura, *Electrochemistry* **2022**, *90*, 27005.
[59] X. Liu, Q. Zhang, C. Du, X. Dou, Y. Zhu, C. Cao, *Mater. Chem. Front.* **2023**.
[60] X. Ye, H. Li, T. Hatakeyama, H. Kobayashi, T. Mandai, N. L. Okamoto, T. Ichitsubo, *ACS Appl. Mater. Interfaces* **2022**, *14*, 56685–56696.
[61] X. Gan, L. Y. S. Lee, K. Wong, T. W. Lo, K. H. Ho, D. Y. Lei, H. Zhao, *ACS Appl. Energ. Mater.* **2018**, *1*, 4754–4765.
[62] Y. Ju, Y. Meng, Y. Wei, X. Bian, Q. Pang, Y. Gao, F. Du, B. Liu, G. Chen, *Chem. Eur. J.* **2016**, *22*, 18073–18079.
[63] S. Zhuo, G. Huang, R. Sougrat, J. Guo, N. Wei, L. Shi, R. Li, H. Liang, Y. Shi, Q. Zhang, P. Wang, H. N. Alshareef, *ACS Nano* **2022**, *16*, 3955–3964.
[64] M. Choi, J. Hwang, H. Setiadi, W. Chang, J. Kim, *J. Supercrit. Fluids* **2017**, *127*, 81–89.
[65] T. Mandai, H. Naya, H. Masu, *J. Phys. Chem. C* **2023**, *127*, 7987–7997.
[66] X. Yu, G. Zhao, C. Wu, H. Huang, C. Liu, X. Shen, M. Wang, X. Bai, N. Zhang, *J. Mater. Chem. A* **2021**, *9*, 23276–23285.
[67] X. Hou, H. Shi, T. Chang, K. Hou, L. Feng, G. Suo, X. Ye, L. Zhang, Y. Yang, W. A. Wang, *Chem. Eng. J.* **2021**, *409*, 128271.
[68] X. Fan, M. Tebyetekerwa, Y. Wu, R. R. Gaddam, X. S. Zhao, *Energy Mater. Adv.* **2022**.
[69] Q. D. Truong, M. Kempaiah Devaraju, Y. Nakayasu, N. Tamura, Y. Sasaki, T. Tomai, I. Honma, *ACS Omega* **2017**, *2*, 2360–2367.

Manuscript received: May 22, 2024
Accepted manuscript online: May 24, 2024
Version of record online: July 5, 2024